Development and Validation of a Micro-CT Compatible Experimental Platform for Frost Formation Studies

A. Labuschagne[a,*], T. Zhu[a], and W. Rohlfs[b]

[a]Department of Thermal and Fluid Engineering, Faculty of Engineering Technology (ET), University of Twente, Drienerlolaan 5, 7522 NB Enschede, The Netherlands
[b]Institute for Heat and Mass Transfer, RWTH Aachen University, Augustinerbach 6, 52062 Aachen, Germany
[*]Corresponding author: a.a.labuschagne@utwente.nl

Abstract

Frost formation on evaporator surfaces continues to limit the performance of air-source heat pumps, yet its three-dimensional evolution under realistic conditions remains insufficiently characterised. Performing such studies inside laboratory Micro-CT systems is technically challenging: the CT scanner's confined space, moisture sensitivity, and strict temperature limits prohibit the use of conventional cooling and air-delivery hardware. Existing frost rigs generally cannot supply independently controlled humidity and temperature at sub-zero conditions within a compact, rotating environment without risking condensation on CT optics. This work presents a Micro-CT-compatible experimental platform that overcomes these limitations by designing a compact, co-rotating architecture in which all air-temperature conditioning and cooling occur inside the CT scanner. The system combines a micro-wind tunnel (MWT) with a counter current copper-in-copper spiral heat exchanger (CiC–SHXC), enabling precise control of temperature, humidity, and flow rate while maintaining all external surfaces above 18 °C for moisture-safe operation. A two-track development strategy was adopted. Track 1 consisted of ex-situ laboratory validation to assess condensation behaviour, frost-growth dynamics, thermal stability, and overall operational safety. Track 2 focuses on the integration strategy to allow the complete MWT, CiC–SHXC, and thermal-oil loop within the CT chamber, supplied by an external psychrometric generator and an LN2-assisted oil chiller. The ex-situ tests demonstrated stable Peltier operation down to –15 °C, reproducible condensation–freezing transitions, and condensation-free external surfaces for coolant temperatures down to approximately −20 °C. Analytical modelling further shows that the CiC–SHXC provides near-isothermal outlet control across all operating modes without unintended subcooling of airstreams. The resulting platform establishes a robust basis for future time-resolved Micro-CT studies of frost evolution and for developing physically grounded frost-growth and defrost models relevant to next-generation heat-pump systems.

Keywords: Frost formation; Micro-CT; Micro-wind tunnel; Counter-current heat exchanger; Psychrometric control; Heat pump

1. Introduction

Frost growth on evaporator surfaces reduces airflow and increases thermal resistance, lowering the coefficient of performance of air-source heat pumps by up to 40% [1, 2]. More efficient frost-control strategies require physically grounded models that capture the transient, heterogeneous nature of frost formation. However, most existing correlations rely on bulk-averaged measurements or simplified assumptions that do not resolve evolving pore-scale structures [3, 4].

X-ray micro-computed tomography (Micro-CT) can resolve frost geometry at the micrometre scale. Synchrotron studies have demonstrated complex dendritic morphologies, pronounced density gradients, and strong anisotropy along the growth direction of frost layers [5]. In their 2018 study, Matsumoto et al. resolved the internal microstructure of frost at high spatial resolution, clearly illustrating that frost is inherently heterogeneous and reinforcing the idea that frost cannot be accurately represented using bulk properties alone.

Despite these useful insights, synchrotron facilities inherently limit experimental throughput, beam time availability, and flexibility in thermal and environmental control. Thus, there remains a serious lack of quality data on frost microstructures. Furthermore, most frost studies grow frost outside the imaging environment and subsequently transfer the sample to the CT rotation stage for scanning [5]. This approach precludes direct observation of growth dynamics and introduces the risk of structural disturbance during handling, mounting, or temperature equilibration.

Laboratory Micro-CT scanners are more accessible and better suited for systematic experimental studies, but they impose their own limitations. These include confined chamber volumes, moisture sensitivity, long scan times (typically 30 min to several hours), and a lack of built-in environmental conditioning. To work within these constraints, several laboratory-scale studies have adopted replica techniques, in which the frost structure is stabilised using polymer solutions or resins prior to scanning. For example, Takayashiki et al. [6] reconstructed frost microstructures by solidifying the ice–air geometry, enabling systematic comparison across operating conditions. However, replica-based approaches yield static representations of frost and cannot capture transient growth, melting, or restructuring processes.

Notably, the authors of replica-based Micro-CT studies explicitly state that true in-situ CT measurements of frost would require frost growth directly inside the CT system itself, which they identify as experimentally challenging [6].

Insight into how such challenges might be addressed can be found in a related but distinct research field: freeze-drying and cryogenic CT. In this context, ice-containing porous materials are imaged during sublimation under controlled thermal and pressure conditions. Hilmer et al. [7], for example, developed a dedicated freeze-drying stage for in-situ μCT measurements, demonstrating that complex cryogenic environments can be successfully integrated into laboratory CT scanners when thermal gradients, moisture management, and mechanical stability are carefully controlled.

Building on this work, Gruber et al. [8] employed in-situ μCT to observe microstructure evolution and the sublimation front during freeze-drying, with samples cooled to −15 °C and −35 °C and scanned continuously over durations on the order of several hours. Scans were performed near atmospheric pressure, and yet the internal ice microstructure remained sufficiently stable throughout these long scan times, indicating that ice-based structures can be imaged without collapse or melting when boundary conditions are well controlled.

These freeze-drying studies demonstrate the technical feasibility of long-duration cryogenic CT imaging of ice-containing materials. However, they rely on static or quasi-static boundary conditions and do not require forced airflow or active humidity control. As a result, their experimental complexity is substantially lower than that of frost-formation experiments, where continuous vapour supply, convective transport, and precise psychrometric regulation are intrinsic to the physical process. When these additional requirements are combined with the geometric, mechanical, thermal and psychrometric constraints of laboratory CT scanners, the experimental challenge becomes substantially more severe.

The Zeiss Xradia Context scanner exemplifies these challenges. The usable space below the imaging head is approximately 250 mm × 100 mm (D × H), served by a single feedthrough port and limited by a 26 kg rotational load capacity. All external surfaces must remain above 18 °C to prevent condensation on the CT scanner interior, and the rotating assembly must remain mechanically balanced during continuous 360° motion. Early attempts to supply precooled air through the required 7 m feed line resulted in 5 to 14 °C/m warming, pressure losses exceeding 4bar, and extensive condensation along exposed sections. These observations confirmed that all cooling and humidity control must occur inside the CT chamber.

These geometric, thermal, and psychrometric constraints impose requirements that no commercial system currently satisfies. A viable platform must sustain sub-zero, humidity-controlled airflows within a millimetre-scale test section, deliver spatially uniform velocity and temperature fields, and maintain unobstructed, low-attenuation X-ray paths. At the same time, it must suppress parasitic condensation throughout the air-delivery network, provide stable Peltier-based surface control, and accommodate multiple sensors positioned close to the imaging region without creating artefacts.

Additional complications arise from routing all electrical, pneumatic, and thermal connections through the single, spatially limited feedthrough port, which imposes both geometric and mechanical constraints. This necessitates strict adherence to minimum bending radii, careful selection of flexible yet pressure- and vacuum-tolerant tubing, and a mechanical layout that avoids micrometre-scale vibrations during rotation. These constraints eliminate many conventional design options used in macroscale frost rigs. Consequently, meeting the combined spatial, thermal, psychrometric, and mechanical requirements within a compact, moisture-sensitive, rotating CT environment demands a fully integrated design approach rather than an assembly of independently optimised modules.

Track 1 employed an ex-situ feasibility configuration or "test-rig" to study condensation behaviour, frost-formation capability, thermal stability, and general operational safety under representative boundary conditions outside the Micro-CT scanner. This simplified setup allowed prototyping of the air-delivery concept, validation of Peltier performance, and identification of critical risks such as coolant viscosity limits, potential condensation points, and thermal-bridging pathways. The insights from this stage then informed the mechanical architecture, heat-exchanger sizing, insulation concept, and psychrometric requirements of the final integrated system.

Track 2 translates these findings into a compact, Micro-CT-compatible design combining a counter-current copper-in-copper spiral heat exchanger (CiC–SHXC), internal air cooling, and independent psychrometric conditioning within the CT scanner. By separating feasibility testing from final integration, the approach reduces project risk, avoids unnecessary fabrication iterations, and ensures that only fully validated components enter the CT environment. In the present paper, only physical results from Track 1 are reported. Track 2 refers to the final Micro-CT-integrated configuration, which is currently under commissioning and is therefore discussed in terms of design intent, thermal–fluidic modelling, and expected operating envelope rather than in-scanner CT measurements.

The primary objective of this paper is the design, implementation, and ex-situ validation of a Micro-CT-compatible frost-formation platform under well-defined thermal, aerodynamic, and psychrometric boundary conditions. While the system is explicitly developed to enable time-resolved in-situ Micro-CT imaging of frost evolution, no CT data are presented here. Instead, this work establishes the experimental and thermal–fluidic foundation upon which such imaging campaigns can be conducted reliably and safely in subsequent studies. The remainder of this paper presents the resulting system architecture, thermal–fluidic modelling, and ex-situ validation results.

2. System Concept and Design Objectives

The system must replicate frost-compatible environmental conditions within the spatial, thermal, and mechanical constraints of the Zeiss Xradia Context. Four objectives guided the design:

- Spatial compatibility: fit within a 250 mm × 100 mm (D × H) envelope while maintaining rotational balance.
- Independent dual-airflow control: humid (0–30 L.min^{-1}) and dry (up to 120 L.min^{-1}) air streams over -2 to 20 °C and 0–100% RH.
- Internal conditioning: provide all cooling and heating inside the CT chamber while maintaining absolute humidity.
- Moisture safety: ensure all exposed surfaces remain above 18 °C.

Fig. 1 shows the overall arrangement. The system consists of a micro-wind tunnel (MWT), a co-rotating counter current copper-in-copper spiral heat exchanger (CiC–SHXC), a tracked umbilical routing pneumatic and electrical lines through the scanning port, and an external psychrometric air & oil chiller.

2.1. Micro-Wind Tunnel Basis

The MWT design follows the coaxial dual-flow concept established previously [9] and illustrated in Fig. 2. The inner stream supplies humid air to the test section, while a dry outer stream forms a thermal shield. This arrangement stabilises the Peltier thermal load, maintains laminar flow through the millimetre-scale test region, and prevents thermal ingress to the test-section. This design, therefore, defines the aerodynamic and thermal requirements that the CiC–SHXC and psychrometric air supply must satisfy.

2.2. Operating Modes and Airflow Strategy

The system naturally operates under two distinct sets of conditions: those required to grow frost in a controlled manner for parameter studies, and those needed to hold the frost structure as stable as possible during long Micro-CT scans. For this reason, the setup is run in two operating modes, each aligned with one of these objectives.

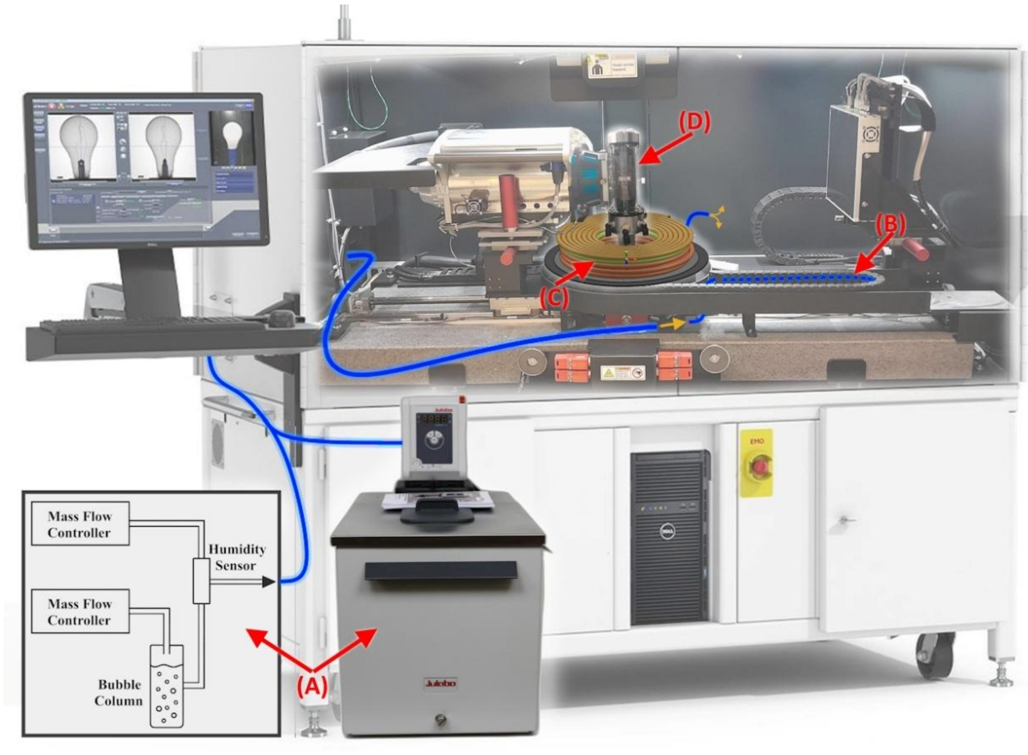

Figure 1. Integrated experimental system: A) psychrometric air generator and oil chiller, B) tracked umbilical, C) CiC–SHXC, D) micro-wind tunnel.

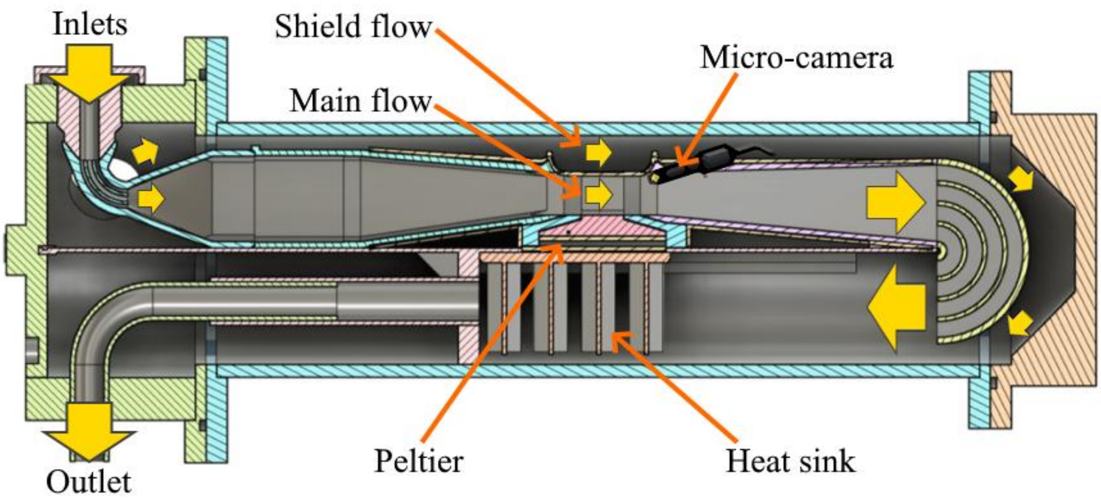

Figure 2. Freezing front observed on the cold plate during Track 1 validation. Red arrows show the direction of front movement.

Mode 1 establishes the environmental conditions for frost formation. The inner stream supplies 0–30 L.min^{-1} of humid air at temperatures between roughly −2 °C and 15 °C, up to 100% RH. The outer shield stream delivers up to 120 L.min^{-1} of dry air at similar temperatures, reducing thermal ingress from the surroundings and maintaining a well-defined psychrometric state. This mode enables repeatable frost growth, supports parameter studies, and is used to prepare a suitable morphology prior to imaging.

Mode 2 is designed to slow or temporarily "freeze" the frost evolution during a CT scan. In this mode, both lines carry dry air for a combined 120–150 L.min^{-1}, subcooled inside the 15 m CiC–SHXC to reach outlet temperatures between approximately −28 °C and −20 °C. The reduced vapour supply and lower thermal potential suppress further growth and limit structural drift over the duration of a scan. This provides the stable conditions required for long Micro-CT acquisitions.

Together, the two modes should allow the same hardware to generate frost under controlled conditions and then hold the resulting structure sufficiently steady for high-resolution imaging.

2.3. Mechanical and Thermal Integration

The MWT is mounted concentrically above the CiC–SHXC on the rotating stage to maximally exploit the cylindrical volume available during 360° rotation and the additional vertical clearance near the feedthrough region, while preserving space for the CiC–SHXC inlet and outlet fittings on both the inner and outer sides of the heat exchanger. The tracked umbilical uses flexible EPDM and PVC tubing for the air supply and PTFE lines for the thermal oil. All tubing remains within the required 30mm bending radius. The CiC–SHXC core (≈13 kg) and MWT assembly (≈3 kg) stay well below the 26 kg load limit, allowing margin for insulation and sensors.

The CiC–SHXC consists of three concentric ”pancake” spirals: two 5m copper-in-copper coils for the Mode 1 humid and shield streams, and a 15 m coil for Mode 2 deep-freeze operation. All layers are embedded in polyurethane and wrapped with graphite-laminated polystyrene sheets incorporating 12W Kapton heating pads, ensuring all external surfaces remain above 18 °C. The thermal oil circuit (nominally –30 °C) is cooled via a LN2-assisted oil chiller outside the chamber.

3. Thermal–Fluidic Design and Modelling

The CiC–SHXC must cool the humid and dry air streams without subcooling, maintain spatial compactness, and limit pressure drop. The cross-section of the final design is seen in Fig. 3. The assembly footprint is approximately 202mm in outer diameter and 92mm in height, with an inner opening of 50mm to accommodate the MWT mounting and connections. This fits comfortably under the CT head while preserving a small clearance to avoid mechanical interference and leaving sufficient space for cabling.

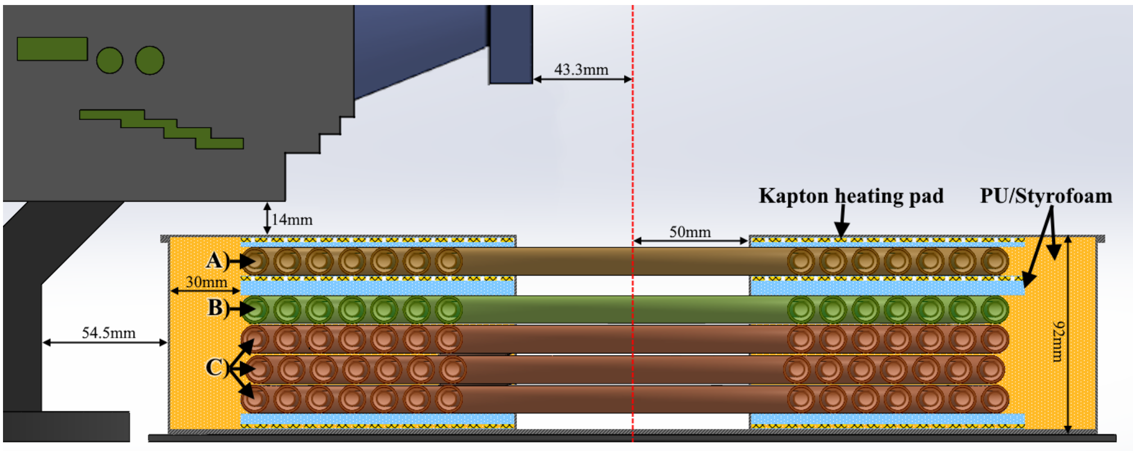

Figure 3. Cross-section of the CiC–SHXC showing tube-in-tube geometry, polyurethane embedding, and insulation layers. The three separate pancakes are indicated by A, B and C.

Each flow path consists of a smaller inner copper tube (6 or 8mm outer diameter) placed concentrically inside a larger tube (10 or 12mm outer diameter). The resulting annular gaps are of the order of 1–2mm, giving mean hydraulic diameters of 2–6mm and heat-transfer surface areas of roughly 0.013–0.019m2 per metre. The three spirals are stacked vertically to form a compact stack of ”pancake” coils, with adequate spacing for polyurethane embedding and structural support.

Analytical sizing used the LMTD method with copper–copper conduction and laminar/transitional air-side convection. Tube diameters, wall thicknesses, and coil lengths were iterated until outlet temperatures approached within 0.5K of the coolant inlet temperature. The resulting overall heat-transfer coefficients and lengths were:

- Mode 1, Pancake A (main/humid): $U = 44.8$ W.m^{-2}.K^{-1}, $L = 2.9$ m,
- Mode 1, Pancake B (shield): $U = 20.3$ W.m^{-2}.K^{-1}, $L = 12.3$ m,
- Mode 2, Pancake C (deep-freeze): $U = 26.7$ W.m^{-2}.K^{-1}, $L = 12.6$ m.

Air-side convective heat transfer coefficients were evaluated using standard internal-flow correlations. For laminar and thermally developing flow, the combined entry-length correlation of Baehr and Stephan [10, 11] was applied, expressed in terms of the Prandtl and Graetz numbers as:

$$\overline{Nu} = \frac{\frac{3.657}{\tanh\left(2.264Gz^{-1/3} + 1.7Gz^{-2/3}\right)} + 0.0499Gz \cdot \tanh\left(Gz^{-1}\right)}{\tanh\left(2.432(Pr/Gz)^{1/6}\right)} \tag{1}$$

where Gz = Re.Pr.D_h/x. For turbulent flow, the Gnielinski correlation [11, 12] was used:

$$Nu = \frac{(f/8)(Re-1000)Pr}{1 + 12.7(f/8)^{1/2}(Pr^{2/3}-1)} \tag{2}$$

The Darcy friction factor *f* was obtained from the Colebrook equation for smooth tubes following standard fluid mechanics references [11, 13, 14]. Fully developed Reynolds numbers ranged between approximately 2300 and 40500 across the three heat-exchanger pancakes (A–C), depending on tube diameter, operating mode, and target flow rate.

Across all configurations, the overall thermal resistance was dominated by the air-side film coefficient. Pressure-drop estimates employed the compressible Darcy–Weisbach formulation with iterative density updates. Predicted Mach numbers remained below 0.22 in all cases, validating the use of incompressible-flow assumptions within the LMTD framework.

For a total mass flow of 3.45 gs^{-1}, the predicted outlet temperatures are 0 °C and 100% RH (Mode 1) and –20 °C (Mode 2). Pressure drops across the coils remain below 1 bar. Embedding the exchanger in polyurethane and incorporating three controlled heating layers maintains all external surfaces above 18 °C, eliminating condensation risk even during long-duration sub-zero operation.

4. Experimental Setup and Procedures

4.1. Track 1: Ex-situ Validation

A simplified ex-situ (outside the CT-scanner) setup was assembled to assess thermal behaviour and condensation risk. Compressed air (7 bar, 20 °C, 5% RH) was humidified via a glass bubble column (yielding ≈88% RH at 10 °C). In this configuration, both the inner and outer annular airstreams were moist but sub-saturated, providing representative conditions for condensation and frosting, but without full independent psychrometric control.

Cooling in Track 1 was provided by a 50% glycol–water mixture circulated through a commercial 30-plate heat exchanger. Glycol was selected as a readily available, though not ideal, surrogate coolant for ex-situ feasibility testing, enabling safe sub-zero operation without introducing the handling, safety, and integration constraints associated with thermal oils or cryogenic systems. Its use was intentionally limited to Track 1 to validate general thermal behaviour, condensation control, and operational robustness, rather than to represent the final coolant choice for CT-integrated operation.

For Mode 1, the glycol loop was operated near 0 °C, while a dry-ice bath enabled deeper Mode 2 testing with nominal glycol temperatures down to –22 °C. As anticipated, the increased viscosity and partial freezing of the glycol at these temperatures led to limited mixing and eventual flow restriction, but still allowed a partial assessment of achievable air temperatures and condensation behaviour within the micro-wind tunnel.

Instrumentation included the TEC-1089 Peltier controller, a PT1000 sensor on the cold plate, a 10kΩ NTC thermistor on the hot side, auxiliary thermocouples, and a miniature micro-camera (OV6948). Fig. 4 illustrates the configuration, including the makeshift dry-ice subcooler and insulated/ventilated hoses.

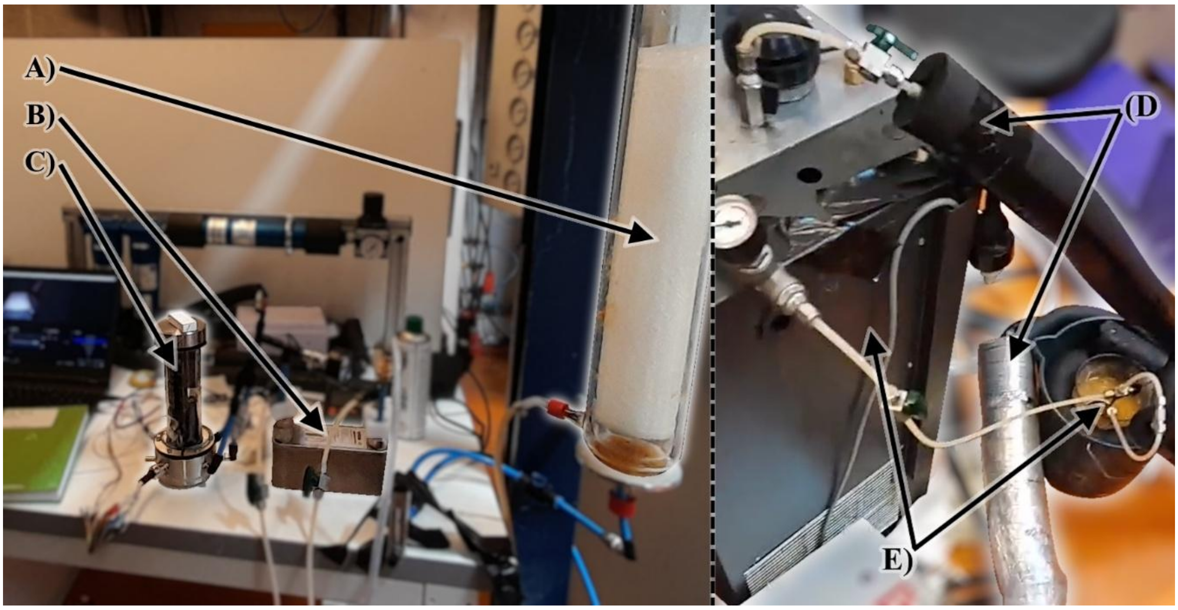

Figure 4. Ex-situ Track 1 setup: A) bubble column, B) plate heat exchanger, C) micro-wind tunnel, D) insulated and dry-air ventilated hoses, E) glycol chiller and dry-ice subcooler bath.

4.2. Track 2: CT-Compatible System Concept and Psychrometric Control

Track 2 implements the full CiC–SHXC, LN2-cooled thermal oil loop, and dual-stream psychrometric generator. Dry air from the compressed-air network is first conditioned using a membrane dryer to achieve very low humidity. A fraction of this air is then bubbled through a temperature-controlled water bath to generate a saturated stream. Mass-flow controllers blend the dry and saturated streams to achieve the desired humidity level.

A Rotronic HF5 transmitter with a HC2 probe measures temperature, relative humidity, and dew point, enabling closed-loop control of the psychrometric state. Dew point is conserved through the lines as long as wall temperatures remain above this value; any colder sections would remove moisture and bias the delivered air drier than intended. For this reason, all wetted lines are insulated and kept above dew point until they reach the CiC–SHXC, where controlled cooling to the target test temperature occurs.

At the time of writing, Track 2 represents the fully designed and modelled CT-compatible configuration; its description here is intended to define the achievable operating space and experimental capabilities rather than to present in-scanner measurement results. Table 1 further lists the planned instrumentation for the integrated system. The combination of PT1000s, differential pressure transducer, humidity sensors, and mass-flow controllers allows detailed tracking of the thermal and psychrometric state at each stage of the MWT.

Table 1. Planned instrumentation for the CT-compatible integrated system [15].

Parameter	Sensor Type	Measurement Location
Temperature	PT1000 (IST P1K0.161.6W)	Cold plate (3×), inlet/outlet air, Peltier hot side
Pressure	Setra ASL1-250LD	Across the test section
Humidity	Rotronic HF5 + HC2 probe	Air-mixer outlet (closed-loop control)
RH/Temperature	Telaire ChipCap 2-SIP	Inside MWT and outlet region
Flow rate	Mass-flow controller	Main and shield air lines

5. Results and Discussion

5.1. Thermal Stability and Condensation Behaviour

During Track 1 validation, the Peltier module maintained stable regulation with a hot–cold temperature difference of $\approx$50K. In steady operation, the cold plate reached − 15 °C while the hot side stabilised near 19 °C. Condensation began 18s after the plate cooled past − 10 °C, initially appearing as a diffuse whitening of the aluminium surface. Within approximately 2 min distinct droplets formed, and by 10 min, a wide droplet-size distribution (around 4–18 mm in diameter) covered the surface. This rapid nucleation followed by growth and coalescence into a broad droplet-size distribution is consistent with prior droplet condensation/freezing studies [16].

Droplet coalescence was not uniform. Larger droplets tended to accumulate near the edges of the plate, especially the top and bottom, where local subcooling is expected to be stronger due to the geometry of the cold block and underlying insulation, and to a lesser extent, gravity. The side-edges were somewhat warmer than the top/bottom due to thinner insulation, leading to thermal leakage. Such spatial non-uniformity is widely reported and is commonly linked to local temperature gradients, wettability, and gravity-driven redistribution, which together bias droplet growth and coalescence toward colder regions and edges [16, 17].

Freezing initiated at ≈21 min along the edges and propagated inward and from top-left to bottom-right, consistent with higher local supercooling near the boundaries. The freezing front advanced rapidly across the 1cm2 surface and completed within roughly 15 s. Fig. 5 shows an example frame capturing the advancing front alongside indications of the propagation direction. Preferential nucleation at colder zones followed by rapid propagation through neighbouring droplets via ice-bridging is consistent with microscopic observations of early frosting/freezing dynamics on cooled surfaces [18, 19].

These observations confirm that the ex-situ configuration reproduces frost nucleation, freezing-front propagation, and spatial growth patterns that are consistent with those reported in the literature under comparable operating conditions. This establishes that the experimental platform generates physically representative frosting behaviour, and therefore provides a suitable basis for future time-resolved in-situ Micro-CT studies aimed at capturing the three-dimensional evolution of these well-known phenomena rather than isolated snapshots.

5.2. Frost Growth During Deep Cooling

Mode 2 began at 34 min. As the glycol bath cooled from 0 to –22 °C, the dry-air temperature decreased gradually and reached –4 °C by 48 min, after which glycol viscosity became too high and flow choking occurred. During this period, the frost layer that formed during Mode 1 continued to evolve, but at a noticeably reduced rate. The extent to which this apparent stabilisation can be attributed specifically to Mode 2 operation cannot be isolated conclusively, as frost growth rates are already known to decrease naturally with increasing frosting time [4].

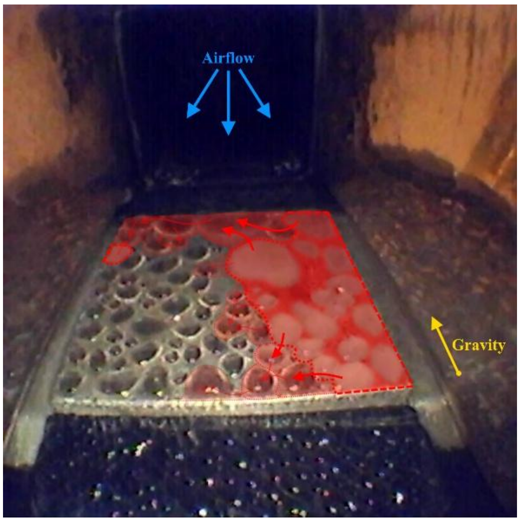

Figure 5. Freezing front observed on the cold plate during Track 1 validation. Red arrows show the direction of front movement.

The embedded micro-camera also revealed thicker frost deposits on the leading edges and frontal surfaces of the plate, where the airflow first impinges, and local subcooling is higher. The downstream region showed thinner, more uniform frost. Preferential frosting at leading edges under forced convection has been reported under heat-pump-relevant operating conditions and is generally attributed to locally enhanced heat transfer and temperature gradients [19].

Although individual crystal shapes could not be resolved, the overall lack of texture and opacity changes looked promising. Fig. 6 shows selected frames illustrating the morphological evolution during the Mode 1 to Mode 2 transition.

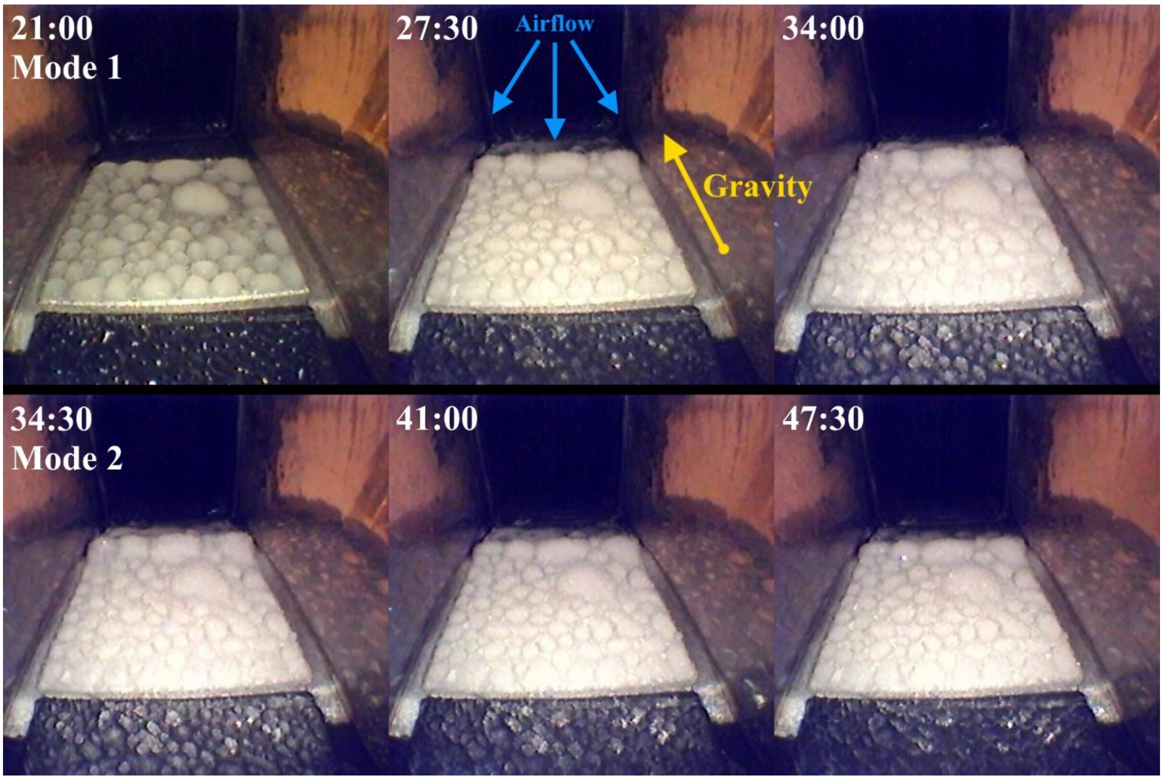

Figure 6. Frost evolution during Mode 1 and Mode 2 operation with experimental time shown in mm:ss.

5.3. CT-Environmental Safety

Using tube insulation and dry-air ventilated jacket isolation strategies, all external surfaces remained above 18 °C, preventing condensation on the MWT housing and exposed tubing. No vibration, leakage, or external icing was observed. The insulation concept and thermal shielding strategy are therefore adequate for safe CT integration. At the coldest stable condition tested (glycol near –22 °C), the air stream in the test section reached –4 °C without inducing condensation on external parts. Replacing glycol with a low-viscosity thermal oil like Therminol® D-12 is expected to enable deeper cooling without flow choking and to extend the operating range towards the targeted Mode 2 air temperatures.

6. Conclusions and Outlook

A Micro-CT compatible frost-formation platform has been developed and validated ex-situ. The co-rotating CiC–SHXC will provide accurate air-temperature control within the confined CT chamber while maintaining moisture-safe external surfaces. Track 1 experiments confirmed stable Peltier operation, predictable condensation–freezing sequences, and effective condensation suppression using insulation and dry-air ventilation strategies. Thermal–fluidic modelling verified that the CiC–SHXC can deliver the required near-isothermal outlet control in all operating modes.

Track 2 will integrate the full system into the CT scanner, including closed-loop psychrometric control and an LN2-assisted thermal-oil chiller capable of supplying coolant near −30°C. In its final configuration, the system will provide mean airflow velocities of 0.5–5 ms-1 with temperatures between -25 and 23°C and relative humidity between 0.5% and 99%. The Peltier stage can regulate the cold-plate temperature between approximately -50 and 50°C, depending on the imposed air temperature. Once operational, the platform will enable time-resolved in-situ Micro-CT imaging of frost growth and melting under this wide range of well-characterised boundary conditions, supporting the development of physically grounded models for frost evolution in next-generation heat-pump systems.

While no Micro-CT data are analysed in the present study, the structure–property evaluation workflow intended for future in-scanner measurements is already established. In earlier work [20], a finite-element-based framework was developed to extract effective thermal conductivity, vapour diffusivity, and the Labuschagne Structural Diffusion Factor (LSDF) from three-dimensional urea crystal reconstructions.

Once the integrated system is commissioned, reconstructed frost volumes will be processed using the same workflow (denoising, greyscale segmentation to ice–air phase fields, meshing, and solution of steady conduction and diffusion problems). This will link controlled in-situ imaging directly to quantitative structure–property evaluation, including effective conductivity, -diffusivity, and LSDF profiles along the sample height.

Acknowledgements

ChatGPT (OpenAI) was used to assist with language clarity. All scientific content was produced by the authors.

References

[1] W. Wang, Y. C. Feng, J. H. Zhu, L. T. Li, Q. C. Guo, and W. P. Lu, "Performances of air source heat pump system for a kind of mal-defrost phenomenon appearing in moderate climate conditions," *Applied Energy*, vol. 112, pp. 1138–1145, 2013.
[2] X.-M. Guo, Y.-G. Chen, W.-H. Wang, and C.-Z. Chen, "Experimental study on frost growth and dynamic performance of air source heat pump system," *Applied Thermal Engineering*, vol. 28, no. 17–18, pp. 2267–2278, 2008.
[3] M. Song and C. Dang, "Review on the measurement and calculation of frost characteristics," *International Journal of Heat and Mass Transfer*, vol. 124, pp. 586–614, 2018.
[4] A. Leoni, M. Mondot, F. Durier, R. Revellin, and P. Haberschill, "Frost formation and development on flat plate: Experimental investigation and comparison to predictive methods," *Experimental Thermal and Fluid Science*, vol. 88, pp. 220–233, 2017.
[5] R. Matsumoto, T. Uechi, and Y. Nagasawa, "Three-dimensional microstructure of frost layer measured by using X-ray CT," *Journal of Thermal Science and Technology*, vol. 13, JTST0014, 2018.
[6] M. Takayashiki, K. Nishimura, A. Sciazko, T. Okabe, J. Taniguchi, and N. Shikazono, "Three-dimensional reconstruction of frost structure by replica method," *International Journal of Heat and Mass Transfer*, vol. 196, 123280, 2022.
[7] M. Hilmer, S. Gruber, and P. Foerst, "Development of a freeze-drying stage for in-situ μ-CT measurements," *Processes*, vol. 8, no. 7, p. 869, 2020.
[8] S. Gruber, N. Vorhauer-Huget, and P. Foerst, "In situ micro-computed tomography to study microstructure and sublimation front during freeze-drying," *Food Structure*, vol. 29, 100213, 2021.
[9] A. Labuschagne, T. Zhu, and W. Rohlfs, "Design and validation of a micro-wind tunnel for in-situ frost formation imaging in a micro-CT scanner," in *Proceedings of the 11th International Symposium on Turbulence, Heat and Mass Transfer (THMT11)*, Begell House, 2025.
[10] H. D. Baehr and K. Stephan, *Heat Transfer*, 2nd ed., Springer, Berlin, 2006.
[11] F. P. Incropera, D. F. DeWitt, T. L. Bergman, and A. S. Lavine, *Fundamentals of Heat and Mass Transfer*, 8th ed., Wiley, Singapore, 2017.
[12] V. Gnielinski, "New equations for heat and mass transfer in turbulent pipe and channel flow," *International Chemical Engineering*, vol. 16, pp. 359–368, 1976.
[13] B. R. Munson, D. F. Young, T. H. Okiishi, and W. W. Huebsch, *Fundamentals of Fluid Mechanics*, 6th ed., Wiley, Hoboken, NJ, 2009.
[14] R. W. Fox, P. J. Pritchard, and A. T. McDonald, *Introduction to Fluid Mechanics*, 7th ed., Wiley, Hoboken, NJ, 2009.
[15] I. Peetam, V. van Krimpen, and A. Labuschagne, "Uncertainty analysis and sensor integration for a micro-wind tunnel frost experiment in a CT environment," in *SET Student Conference Proceedings*, University of Twente, 2025.
[16] E. Harges, L. Cremaschi, and B. Adanur, "Distribution, coalescence, and freezing characteristics of water droplets on surfaces with different wettabilities under subfreezing convective flow," *Applied Thermal Engineering*, vol. 182, 116052, 2021.
[17] H. Kim, D. Kim, H. Jang, D. R. Kim, and K.-S. Lee, "Microscopic observation of frost behaviors at the early stage of frost formation on hydrophobic surfaces," *International Journal of Heat and Mass Transfer*, vol. 97, pp. 861–867, 2016.
[18] E. N. Harges and L. Cremaschi, "Effects of crystal formation on the initial frost thickness and density on cold surfaces," *International Journal of Refrigeration*, vol. 136, pp. 82–93, 2022.

[19] E. N. Harges, *Experimental and Analytical Investigation of Early Frost Growth on Surfaces with Varying Wettability under Typical Heat Pump Operating Conditions*, Ph.D. dissertation, Auburn University, 2021.
[20] A. Labuschagne, T. Zhu, and W. Rohlfs, “Micro-CT investigation of urea crystal structures for frost analysis,” *International Journal of Thermal Sciences*, vol. 214, 2025.